Faraday Discussions

Cite this: DOI: 10.1039/c9fd00046a

PAPER

Nonadiabatic dynamics with quantum nuclei: simulating charge transfer with ring polymer surface hopping†

Soumya Ghosh, ‡*[a] Samuele Giannini,[a] Kevin Lively§[a] and Jochen Blumberger[ab]

Received 24th April 2019, Accepted 7th June 2019
DOI: 10.1039/c9fd00046a

Investigation of many electronic processes in molecules and materials, such as charge and exciton transport, requires a computational framework that incorporates both non-adiabatic electronic effects and nuclear quantum effects, in particular at low temperatures. We have recently developed an efficient semi-empirical fewest switches surface hopping method, denoted fragment orbital-based surface hopping (FOB-SH), that was tailored towards highly efficient simulation of charge transport in molecular materials, yet with nuclei treated classically. In this work, we extend FOB-SH and include nuclear quantum effects by combining it with ring-polymer molecular dynamics (RPMD) in three different flavours: (i) RPSH with bead approximation (RPSH-BA) as suggested in Shushkov *et al.*, *J. Chem. Phys.*, 2012, **137**, 22A549, (ii) a modification of (i) denoted RPSH with weighted bead approximation (RPSH-wBA) and (iii) the isomorphic Hamiltonian method of Tao *et al.*, *J. Chem. Phys.*, 2018, **148**, 10237 (SH-RP-iso). We present here applications to hole transfer in a molecular dimer model and analyze detailed balance and internal consistency of all three methods and investigate the temperature and driving force dependence of the hole transfer rate. We find that RPSH-BA strongly underestimates and RPSH-wBA overestimates the exact excited state population, while SH-RP-iso gives satisfactory results. We also find that the latter predicts a flattening of the rate *vs.* driving force dependence in the Marcus inverted regime at low temperature, as often observed experimentally. Overall, our results suggest that FOB-SH combined with SH-RP-iso is a promising method for including zero point motion and tunneling in charge transport simulations in molecular materials and biological systems.

[a]*Department of Physics and Astronomy, University College London, Gower Street, London WC1E 6BT, UK. E-mail: soumya.ghosh@theochem.rub.de*

[b]*Institute for Advanced Study, Technische Universität München, Lichtenbergstrasse 2a, D-85748 Garching, Germany*

† Electronic supplementary information (ESI) available: The supporting information consists of two figures that illustrate the increase in radius of gyration at 100 K compared to 300 K. See text for more details. See DOI: 10.1039/c9fd00046a

‡ Present address: Lehrstuhl fuer Theoretische Chemie, Ruhr-Universität Bochum, Bochum, Germany.

§ Present address: Max Planck Institute for the Structure and Dynamics of Matter, Hamburg, Germany.

1 Introduction

Nonadiabatic processes dictate several photochemical and photophysical phenomena in a wide variety of systems ranging from small molecules to solids, including complex biological and organic semiconductors. Simulating nonadiabatic processes requires time evolution of multiple electronic states as well as a proper description of nuclear (ionic) motion. Full quantum mechanical description of both electronic and nuclear motion is prohibitively expensive and only possible for few atoms. Hence, one seeks a compromise where the electronic motion is treated quantum mechanically while the nuclear motion is treated classically, resulting in the so-called nonadiabatic mixed quantum classical (NA-MQC) dynamics. Several approaches have been developed over the years that can be loosely classified as NA-MQC dynamics including trajectory surface hopping (TSH),[1–19] mean-field Ehrenfest,[20–23] mixed quantum-classical Liouville equation (QCLE),[24–26] the mapping approach,[27–31] multiple spawning,[32,33] nonadiabatic Bohmian dynamics[34,35] and coupled-trajectories mixed quantum-classical method.[36]

Conceptual simplicity and straightforward implementation has made TSH one of the most popular NA-MQC methods. In TSH, one runs a swarm of independent classical trajectories to model time evolution of a nuclear wave packet and a stochastic algorithm is employed to incorporate transitions from the active adiabatic state to another one. Different flavours of TSH have been developed over the years depending on how and when the stochastic jumps are employed. In one of the most popular approaches, known as the fewest switch surface-hopping algorithm (FSSH),[2] the state switch is associated with an instantaneous jump from one adiabatic surface to another based on hopping probability. The hopping probability in FSSH is calculated from the electronic density matrix and the nonadiabatic coupling between the two states in such a fashion so that one needs a minimum number of state switches in order to maintain consistency between the electronic (adiabatic) and surface population. While the classical description of nuclei is adequate in many cases, the incorporation of nuclear quantum effects like vibrational tunneling might become important in certain scenarios, like charge transfer/transport in organic semiconductors at low temperatures.[37] In the context of TSH, this problem has been addressed in two different ways. In the army ants tunneling method,[38] proposed by Truhlar's group, an effective tunneling coordinate is defined beforehand based on internal coordinates and the tunneling probability is evaluated semi-classically. The population of the trajectories is modulated depending on the tunneling probability. Alternatively, one can introduce nuclear quantum effects employing the framework of ring polymer molecular dynamics (RPMD).[39–42] In this context, Shushkov, Li and Tully[43] proposed two closely related variants – ring polymer surface hopping with bead approximation (RPSH-BA) and ring polymer surface hopping with centroid approximation (RPSH-CA). In these methods each replica/bead is propagated on its own adiabatic surface (ground or excited) while the electronic Schrödinger equation is generated either from bead-averaged quantities (RPSH-BA) or from the quantities evaluated at the ring polymer centroid position (RPSH-CA). Shakib *et al.*[44] demonstrated the critical role played by zero-point energy corrections and nuclear tunneling effects by applying RPSH-CA on model potential energy

surfaces. A conceptually different approach to combine RPMD with TSH has been developed by Lu and Zhou,[45,46] known as path integral molecular dynamics with surface hopping (PIMD-SH), where each bead may occupy a different state with the aim to compute thermal averages for observables. More recently, yet another approach has been proposed by Tao, Shushkov and Miller[47] in order to introduce nuclear quantum effects in conjunction with NA-MQC dynamics. In this approach, known as the isomorphic Hamiltonian method, one constructs an effective Hamiltonian from the diabatic electronic Hamiltonian of each bead that preserves the quantum Boltzmann statistics. Within this mean field approach, one can combine different non-thermostatted path integral based methods like RPMD and centroid molecular dynamics (CMD)[48,49] with various NA-MQC approaches like TSH and QCLE.

We have recently introduced an efficient fewest switches surface hopping method with classical nuclei, termed fragment orbital-based surface hopping (FOB-SH),[50] that was tailored towards efficient simulation of charge transport in large condensed phase systems through expansion of the charge carrier wavefunction in a localized (or site) basis of molecular frontier orbitals. The merit of this explicit charge propagation method is that it can be used in regimes where traditional theoretical approaches, such as charge carrier hopping or band theory no longer apply, *e.g.* in many organic semiconductors, DNA *etc.*[51] In a first series of tests, we have shown that the method could reproduce H_{ab}, λ and ΔG dependence for charge transfer in a dimer in the nonadiabatic regime in good agreement with Marcus theory.[52] Interestingly, we observed a crossover from activated charge transfer to Rabi-type ultrafast charge relaxation in the limit of large electronic couplings ($H_{ab} = \lambda/2$). In chains of molecules modeling organic semiconductors, this regime is characterized by a crossover from activated hopping of a localized charge (small polaron) to band-like transport of a delocalized charge (delocalized polaron),[53] as observed sometimes experimentally.[54]

Explicit simulations of charge transfer/transport dynamics at low temperatures are of general interest. Many experimental studies on charge mobility in (bio)organic materials have been carried out in a wide temperature range to probe the carrier mechanism, from temperatures as low as a few 10 K to room temperature.[55] For ultrapure organic crystals a power-law decay of electron mobility with temperature has been observed, $\mu = T^{-\eta}$. Interestingly, rather different values for the decay constant have been reported for similar materials ranging from $\eta = 1$ to $\eta = 3$. Preliminary results indicate that while FOB-SH reproduces experimental mobilities at high temperatures and qualitatively reproduces the power-law decay at low temperatures, but the decay coefficient η is underestimated, most likely because of missing nuclear tunneling and zero point energy (ZPE) effects. Hence, it would be extremely desirable to include these effects in the FOB-SH method.

In this work we report the implementation of the RPSH-BA method and a particular flavour of the isomorphic Hamiltonian method that combines RPMD with TSH, known as SH-RP-iso, in the context of FOB-SH simulations. We investigate the ability of these methods to preserve two of the most desirable features in any TSH simulation, internal consistency and detailed balance (see Section 4.1 for details), for a model problem involving a charge transfer reaction between two "ethylene-like" molecules in a bath of Ne atoms. The parameters employed in this model system are chosen diligently in order to mimic the

parameter regime relevant for charge transfer/transport in organic semiconductor materials.[56]

We observe that RPSH-BA suffers from very few successful hops resulting in a severe underestimation of the excited state population. In order to rectify this issue, we propose a modification of the RPSH-BA method, denoted here as ring polymer surface hopping with weighted bead approximation (RPSH-wBA) that increases the number of successful hops but overestimates the excited state population. On the other hand, the excited state population extracted from SH-RP-iso simulations is found to be much closer to the "exact" excited state population. Based on these results we chose to compute charge transfer rate constants with SH-RP-iso and FOB-SH methods at different temperatures. In contrast to the rate constants obtained from simulations with classical nuclei, the charge transfer rate constants extracted from ring polymer simulations show much weaker temperature dependence, a probable consequence of quantum nuclear tunneling at low temperatures. The trends in computed rate constants as a function of temperature are found to be qualitatively consistent with the temperature dependence of Golden rule rate constant expressions where the Franck–Condon factor is derived for classical nuclei or from a quantized spin-boson model. We further investigate the dependence of rate constants on the free energy difference between the reactant and product states. At 100 K, the rate constants extracted from SH-RP-iso simulations demonstrate a clear asymmetry in the curvature due to the lower rate of decrease of rate constants in the Marcus inverted regime, a feature that is indicative of vibrational tunneling effects.

This paper is organized as follows. In Section 2 we briefly describe RPSH-BA, its modification, which we call RPSH-wBA, and the isomorphic Hamiltonian method. Proof of the expressions employed in describing the RPSH-wBA method is given in the Appendix. We also define here the Marcus rate constant expression for charge transfer reactions, along with an analytical expression where the semiclassical Franck–Condon factor is replaced by a quantized version that involves overlap of harmonic oscillator wavefunctions, henceforth described as quantum rate constant. After description of the molecular model, force field parameters and the details of the surface hopping simulations in Section 3, we present and discuss the results of our calculations in Section 4. This analysis is followed by a summary and future directions of our work in Section 5.

2 Theory

2.1 FOBSH

In the recently developed fragment orbital-based (FOB) surface hopping approach, it is assumed that the complicated many-body electron dynamics can be effectively described by a one-particle wavefunction $\Psi(t)$ for an excess charge (electron or electron hole) moving in an effective, time-dependent potential due to the other electrons and classical nuclear motion. The interaction of all other electrons with the charge carrier is included implicitly through a parametrized electronic Hamiltonian. The charge carrier wavefunction $\Psi(t)$ is expanded in a basis of localized, non-orthogonal fragment orbitals, $\{\varphi_m\}$, that are located on M "sites" of a molecular system and mediate the charge transfer. The fragment orbital basis is orthogonalized using Löwdin orthogonalization. The carrier wavefunction in the orthogonal fragment orbital basis $\{\phi_l\}$ then reads

$$\Psi(t) = \sum_{l=1}^{M} u_l(t)\phi_l(\mathbf{R}(t)). \quad (1)$$

In this basis, the time-dependent Schrödinger equation (TDSE) takes the familiar form,

$$i\hbar\dot{u}_k(t) = \sum_{l=1}^{M} u_l(t)(H_{kl} - i\hbar d_{kl}), \quad (2)$$

where H_{kl} are the elements of the (non-diagonal) electronic Hamiltonian in the $\{\phi_l\}$ basis, $H_{kl} = [\mathbb{H}]_{kl}$, and $d_{kl} = \langle\phi_k|\dot{\phi}_l\rangle$ are the nonadiabatic coupling elements (NACEs). In what follows, we refer to the fragment orbital bases $\{\varphi_l\}$ and $\{\phi_l\}$ as non-orthogonal and orthogonal diabatic bases, respectively, even though the NACEs d_{kl} are in general non-zero, albeit small. The diagonal element $H_{kk} = \langle\phi_k|H|\phi_k\rangle$ is the energy of the excess charge localized on molecule k that can be estimated using a classical force field where molecule k is charged and all the other $M - 1$ molecules are neutral. The off-diagonal term $H_{kl} = \langle\phi_k|H|\phi_l\rangle$ is the electronic coupling matrix elements between the two diabatic states ϕ_k and ϕ_l. In SH molecular dynamics, the nuclear degrees of freedom are propagated on a single adiabatic potential energy surface E_i ($\equiv[\mathbb{H}^{\mathrm{ad}}]_{ii}$), which is obtained by unitary transformation of the diabatic Hamiltonian, $\mathbb{H}$, eqn (3) where $\mathbb{U}$ is the transformation matrix. The corresponding adiabatic states are denoted by $\{\psi_i\}$.

$$\mathbb{H}^{\mathrm{ad}} = \mathbb{U}^{\dagger}\mathbb{H}\mathbb{U} \quad (3)$$

$$\psi_i = \sum_{k=1}^{M} U_{ki}\phi_k \quad (4)$$

The nuclear forces on the adiabatic state i, $\mathbf{F}_{I,i}$, can be obtained from the gradients of the Hamiltonian matrix elements in the diabatic representation using the Hellmann–Feynman theorem,

$$\mathbf{F}_{I,i} = -\nabla_I E_i = -\nabla_I\langle\psi_i|H|\psi_i\rangle = -\left[\mathbb{U}^{\dagger}(\nabla_I\mathbb{H})\mathbb{U}\right]_{ii} \quad (5)$$

where $[\nabla_I\mathbb{H}]_{kl} \equiv \nabla_I H_{kl} = \nabla_I\langle\phi_k|H|\phi_l\rangle$. The last identity in eqn (5) has been shown explicitly in ref. 50. In practice, the gradients of the diagonal and off-diagonal elements are obtained with classical force fields and finite difference of the orbital overlap using the analytic overlap method (AOM),[57] respectively. The probability to hop from the current (active) adiabatic state i to another state j in the Tully's fewest switch algorithm is given by

$$g_{ij} = \max\left[0, \frac{-2\mathrm{Re}\left(a_{ij}^{*}d_{ij}^{\mathrm{ad}}\right)}{a_{ii}}\Delta t\right] \quad (6)$$

where $a_{ij} = c_i^{*}c_j$ is the electronic density matrix, c_i being the expansion coefficients of the wavefunction in the adiabatic basis, $\Psi(t) = \sum_{l=1}^{M} c_i(t)\psi_i(\mathbf{R}(t))$. Importantly, the hopping probabilities depend on the NACEs between the adiabatic states, d_{ij}^{ad}, which is defined as the projection of the nuclear velocity on the adiabatic NACV.

$$d_{ij}^{\mathrm{ad}} = \dot{\mathbf{R}}_I \cdot \mathbf{d}_{I,ij}^{\mathrm{ad}} \tag{7}$$

In the diabatic basis, the adiabatic NACEs are obtained from the temporal change in the transformation matrix and the diabatic NACEs ($d_{kl} \equiv [\mathbb{D}]_{kl}$) of eqn (2).

$$d_{ij}^{\mathrm{ad}} = \left[\mathbb{U}^{\dagger}\mathbb{D}\mathbb{U}\right]_{ij} + \left[\mathbb{U}^{\dagger}\dot{\mathbb{U}}\right]_{ij} \tag{8}$$

An important component of the surface hopping algorithm is velocity rescaling upon a successful hop. It has been shown previously that rescaling the nuclear velocity in the direction parallel to the adiabatic NACV ($\mathbf{d}_{I,ij}^{\mathrm{ad}} = \langle \psi_i | \nabla_I \psi_j \rangle$) improves detailed balance. Using the Hellmann–Feynman theorem, one can reformulate the adiabatic NACV in terms of gradient of the adiabatic Hamiltonian (eqn (10) in ref. 58). Finally, employing the diabatic to adiabatic transformation matrix ($\mathbb{U}$), one can express the adiabatic NACV in a diabatic basis.

$$\mathbf{d}_{I,ij}^{\mathrm{ad}} = \frac{1}{E_j - E_i}\left[\mathbb{U}^{\dagger}(\nabla_I \mathbb{H})\mathbb{U}\right]_{ij} + \left[\mathbb{U}^{\dagger}\mathbb{D}_I\mathbb{U}\right]_{ij} \tag{9}$$

It has been shown in our earlier work[58] that the last term in eqn (9) is numerically small and can be ignored. Hence, the working expression for the adiabatic NACV in the diabatic basis is given by:

$$\mathbf{d}_{I,ij}^{\mathrm{ad}} \approx \frac{1}{E_j - E_i}\left[\mathbb{U}^{\dagger}(\nabla_I \mathbb{H})\mathbb{U}\right]_{ij}. \tag{10}$$

The details of the derivation of the above equation are provided in ref. 58. In Appendix A we provide an alternative derivation of eqn (8) starting from eqn (9).

2.2 Ring polymer surface hopping with bead approximation (RPSH-BA)

In RPMD one performs classical MD with a ring polymer Hamiltonian in the extended phase space at n times the physical temperature. In practice, physical forces are calculated individually on each replica and the spring forces are added separately at each MD time step. The ring polymer Hamiltonian with n beads, each consisting of $\{I\}$ nuclei is written as

$$\mathscr{H}_n = \sum_{\alpha=1}^{n}\left[\sum_{I}\left[\frac{p_{I,\alpha}^2}{2M_I} + \frac{1}{2}M_I{\omega_n}^2(\mathbf{R}_{I,\alpha} - \mathbf{R}_{I,\alpha-1})^2\right] + E_{i,\alpha}(\{\mathbf{R}_I\}_{\alpha})\right] \tag{11}$$

where M_I is the physical mass of the I^{th} nucleus, $\mathbf{p}_{I,\alpha}$ and $\mathbf{R}_{I,\alpha}$ are the momentum and position associated with the I^{th} nucleus of the α^{th} bead, $\omega_n = nk_{\mathrm{B}}T/\hbar$ and $E_{i,\alpha}$ is the ith eigenstate of the α^{th} bead. The corresponding Hamilton's equation of motion is given by:

$$\begin{aligned}\dot{\mathbf{p}}_{I,\alpha} &= -M_I{\omega_{n_{\mathrm{b}}}}^2(2\mathbf{R}_{I,\alpha} - \mathbf{R}_{I,\alpha-1} - \mathbf{R}_{I,\alpha+1}) - \frac{\partial E_{i,\alpha}(\{\mathbf{R}_I\}_{\alpha})}{\partial \mathbf{R}_{I,\alpha}} \\ \dot{\mathbf{R}}_{I,\alpha} &= \frac{\mathbf{p}_{I,\alpha}}{M_I}.\end{aligned} \tag{12}$$

Several attempts have been made to couple TSH with the ring polymer framework. In the RPSH method, proposed by Shushkov *et al.*,[43] the dynamics of each bead is performed on the same adiabatic state ($i_\alpha = i$) determined by the SH algorithm. The corresponding electronic Schrödinger equation is propagated in the adiabatic basis employing the adiabatic energies and adiabatic NACEs that are either averaged over all the beads (RPSH-BA) or computed with the centroid coordinates (centroid approximation). For the bead approximation, the TDSE takes the following form:

$$i\hbar\dot{c}_i = \left[\frac{1}{n}\sum_{\alpha=1}^{n} E_{i,\alpha}\right] c_i - i\hbar\sum_j \left[\frac{1}{n}\sum_{\alpha=1}^{n} d^{\mathrm{ad}}_{ij,\alpha}\right] c_j \tag{13}$$

where $E_{i,\alpha}$ is the energy of the ith eigenstate and $d^{\mathrm{ad}}_{ij,\alpha}$ is the adiabatic NACE corresponding to the α^{th} bead. Using model potential energy surfaces, it has been shown that the bead approximation provides reasonable reactive flux rates even at fairly low temperatures while the centroid approximation is mostly applicable at ambient to high temperatures.

While a direct propagation of the TDSE in the adiabatic basis is numerically challenging due to sudden peaks in the NACEs at avoided crossings, propagation in the diabatic basis is numerically more robust. We first introduce the eigenvector matrix of the bead-averaged diabatic Hamiltonian,

$$\overline{\mathbb{H}} = \frac{1}{n}\sum_{\alpha=1}^{n} \mathbb{H}_\alpha \tag{14}$$

and use it to define the diabatic wavefunction coefficients, $\tilde{\mathbf{u}}(\{\mathbf{R}_{I,\alpha}\})$,

$$\tilde{\mathbf{u}}(\{\mathbf{R}_{I,\alpha}\}) = \overline{\mathbb{U}}\mathbf{c}(\{\mathbf{R}_{I,\alpha}\}). \tag{15}$$

Insertion of eqn (15) in (13) gives the following TDSE for $\tilde{\mathbf{u}}$ (see Appendix for a derivation):

$$i\hbar\dot{\tilde{u}}_k = \sum_l \tilde{u}_l(\tilde{H}_{kl} - i\hbar\tilde{d}_{kl} - i\hbar v_{kl}) \tag{16}$$

where

$$\tilde{H}_{kl} = \left[\overline{\mathbb{U}}\left(\frac{1}{n}\sum_{\alpha=1}^{n}\mathbb{H}^{\mathrm{ad}}_\alpha\right)\overline{\mathbb{U}}^\dagger\right]_{kl} \tag{17}$$

$$\tilde{d}_{kl} = \left[\overline{\mathbb{U}}\left(\frac{1}{n}\sum_{\alpha=1}^{n} d^{\mathrm{ad}}_{ij,\alpha}\right)\overline{\mathbb{U}}^\dagger\right]_{kl} \tag{18}$$

$$v_{kl} = \left[\overline{\mathbb{U}}\dot{\overline{\mathbb{U}}}^\dagger\right]_{kl}. \tag{19}$$

$\mathbb{H}^{\mathrm{ad}}_\alpha$ and $d^{\mathrm{ad}}_{ij,\alpha}$ in eqn (17) and (18) are calculated for each bead using eqn (3) and (8) respectively. As suggested by Shushkov *et al.*,[43] the velocities of all the nuclei are rescaled to conserve the total energy of all the beads:

$$\frac{1}{2}\sum_{\alpha}\sum_{I} M_I\left(\dot{R}'^2_{I,\alpha} - \dot{R}^2_{I,\alpha}\right) + n\Delta\tilde{E}_{ij} = 0, \tag{20}$$

where $\dot{\mathbf{R}}'_{I,\alpha}$ is the rescaled velocity of the I^{th} nucleus of the α^{th} bead and $\Delta\tilde{E}_{ij}$ is the difference in the average potential energies of the new and old state.

$$\Delta\tilde{E}_{ij} = \frac{1}{n}\sum_{\alpha=1}^{n}\left(E_{j,\alpha} - E_{i,\alpha}\right) \tag{21}$$

The rescaling of velocities is performed in the direction of the adiabatic NACV of each bead, $\mathbf{d}^{\text{ad}}_{I,ij}(\{\mathbf{R}_I\}_\alpha)$.

$$\dot{\mathbf{R}}'_{I,\alpha} = \dot{\mathbf{R}}_{I,\alpha} + \gamma\frac{\mathbf{d}^{\text{ad}}_{I,ij}(\{\mathbf{R}_I\}_\alpha)}{M_I} \tag{22}$$

2.3 Ring polymer surface hopping with weighted bead approximation (RPSH-wBA)

As explained in Section 4.1, the dynamics with RPSH-BA underestimates the excited state population due to very few successful hops. In an attempt to rectify this problem we introduce here a modification of the BA, denoted weighted bead approximation, wBA. It is based on the observation that in the BA the adiabatic (eigen) energies and the NACEs between the adiabatic states of each bead are calculated first and then averaged. An alternative procedure is to first define the "average" adiabatic states and then consistently calculate the NACVs and NACEs between them. In this formulation, the average adiabatic eigenstates $\{|i\rangle,|j\rangle\}$ diagonalize the average diabatic Hamiltonian, $\overline{\mathbb{H}}$. The TDSE within the RPSH-wBA approximation takes a form analogous to eqn (16) where $\tilde{H}_{kl}$ is replaced by $\overline{H}_{kl} = [\overline{\mathbb{H}}]_{kl}$ while $\overline{d}_{kl}(= \overline{\mathbb{U}}\overline{\mathbb{D}}^{\text{ad}}\overline{\mathbb{U}}^{\dagger})$ replaces $\tilde{d}_{kl}$.

$$i\hbar\dot{\overline{u}}_k = \sum_l \overline{u}_l(\overline{H}_{kl} - i\hbar\overline{d}_{kl} - i\hbar v_{kl}) \tag{23}$$

The matrix elements of $\overline{\mathbb{D}}^{\text{ad}}$, denoted by $\bar{d}^{\text{ad}}_{ij}$, are given by

$$\begin{aligned}\bar{d}^{\text{ad}}_{ij} = \frac{1}{n\Delta\overline{E}_{ij}}\sum_{\alpha}\sum_{i_\alpha}\sum_{j_\alpha}\Delta E_{i_\alpha j_\alpha}\langle i|i_\alpha\rangle\langle j_\alpha|j\rangle \\ \left[\mathbb{U}^{\dagger}_{\alpha}\dot{\mathbb{U}}_{\alpha} + \mathbb{U}^{\dagger}_{\alpha}\mathbb{D}_{\alpha}\mathbb{U}_{\alpha}\right]_{i_\alpha j_\alpha}\end{aligned} \tag{24}$$

where $\Delta\bar{E}_{ij}$ is the difference in energy between the j^{th} and i^{th} eigenstates of $\overline{\mathbb{H}}$ and $\Delta E_{i\alpha j\alpha}$ is the energy difference between the $j_\alpha{}^{\text{th}}$ and $i_\alpha{}^{\text{th}}$ eigenstates of the α^{th} diabatic Hamiltonian $\mathbb{H}_\alpha$.

$$\begin{aligned}\Delta\overline{E}_{ij} &= \left[\overline{\mathbb{U}}^{\dagger}\overline{\mathbb{H}}\overline{\mathbb{U}}\right]_{jj} - \left[\overline{\mathbb{U}}^{\dagger}\overline{\mathbb{H}}\overline{\mathbb{U}}\right]_{ii} \\ \Delta E_{i_\alpha j_\alpha} &= E_{j,\alpha} - E_{i,\alpha}\end{aligned} \tag{25}$$

Note that both eqn (16) and (23) reduce to eqn (2) in the limit $n = 1$. As shown in the Appendix the expression for $\bar{d}^{\text{ad}}_{ij}$ is derived from the adiabatic NACVs, $\bar{\mathbf{d}}^{\text{ad}}_{I\alpha,ij}$, corresponding to the average diabatic Hamiltonian, $\overline{\mathbb{H}}$. These adiabatic NACVs

can be expressed in terms of the NACV between the adiabatic states ($\{|i_\alpha\rangle,|j_\alpha\rangle\}$) of each bead with the use of the Hellmann–Feynman theorem by projecting $\{|i\rangle,|j\rangle\}$ onto $\{|i_\alpha\rangle,|j_\alpha\rangle\}$. The working form of the adiabatic NACV is given by:

$$\overline{\mathbf{d}}^{\mathrm{ad}}_{I_\alpha,ij} \approx \frac{1}{n\Delta\overline{E}_{ij}} \sum_{i_\alpha}\sum_{j_\alpha} \langle i|i_\alpha\rangle\langle j_\alpha|j\rangle \left[\mathbb{U}^\dagger_\alpha(\nabla_{I_\alpha}\mathbb{H}_\alpha)\mathbb{U}_\alpha\right]_{i_\alpha j_\alpha}. \tag{26}$$

As will be seen later, this modification significantly increases excited state population. Although RPSH-wBA is conceptually simple and results in a larger number of hops compared to RPSH-BA, there is no simple way to formulate a consistent velocity rescaling scheme, since each bead evolves on its own adiabatic surface while the electronic dynamics is dictated by the eigenvalue spectrum of the average diabatic electronic Hamiltonian. In our current formulation, we treat an attempted hop in two steps. We first check whether the ring polymer has enough kinetic energy to compensate for change in the average adiabatic energies of the two surfaces ($\Delta\tilde{E}_{ij}$, eqn (21)). If this criterion is met then we rescale the velocities using eqn (22) and (20) where $\mathbf{d}^{\mathrm{ad}}_{I,ij}(\{\mathbf{R}_I\}_\alpha)$ is replaced with $\overline{\mathbf{d}}^{\mathrm{ad}}_{I_\alpha,ij}$ (eqn (26)) and $\Delta\tilde{E}_{ij}$ is replaced with $\Delta\bar{E}_{ij}$ (eqn (25)), respectively. In the next section we summarize the recently proposed isomorphic Hamiltonian method where both the electronic dynamics and the nuclear dynamics are performed with the same Hamiltonian.

2.4 Isomorphic Hamiltonian (SH-RP-iso)

In the isomorphic Hamiltonian method, the matrix elements of the diabatic Hamiltonians of all the beads are combined together to generate the isomorphic Hamiltonian in such a way that classical Boltzmann sampling of this Hamiltonian preserves the quantum Boltzmann statistics of the physical system. The method has been described extensively in the original article.[47] Here we present only the key equations. The diagonal elements of the potential energy matrix, $\mathbb{V}^{\mathrm{iso}}$, of the isomorphic Hamiltonian are the same as the diagonal elements of $\overline{\mathbb{H}}$,

$$V^{\mathrm{iso}}_i = \frac{1}{n}\sum_{\alpha=1}^{n} [\mathbb{H}_\alpha]_{ii}, \tag{27}$$

but the condition on preserving the quantum Boltzmann statistics requires a more involved average for the off-diagonals,

$$\left(K^{\mathrm{iso}}_{kl}\right)^2 = \frac{1}{\beta^2} a \cosh^2\left(\frac{1}{2}\mathrm{e}^{\frac{1}{2}\beta\left(V^{\mathrm{iso}}_k + V^{\mathrm{iso}}_l\right)}\mu_{kl}\right) - \frac{1}{4}\left(V^{\mathrm{iso}}_l - V^{\mathrm{iso}}_k\right)^2, \tag{28}$$

where, for a 2-level system,

$$\mu_{kl} = \mu_{12} = \mathrm{tr}_{\mathrm{e}}\left[\prod_{\alpha=1}^{n} \mathrm{e}^{-\beta_n \mathbb{H}_\alpha}\right]. \tag{29}$$

In the above expressions, $\beta = 1/(k_{\mathrm{B}}T)$, and $\beta_n = \beta/n$. The isomorphic Hamiltonian method differs fundamentally from RPSH-BA and RPSH-wBA in the way how the nuclear and electronic dynamics are performed. In the previous two methods, the physical forces for nuclear dynamics are calculated separately for each bead while

the electronic dynamics is performed by an effective electronic Hamiltonian that includes contributions from all the beads. In SH-RP-iso, both the nuclear and electronic dynamics involve the same isomorphic Hamiltonian. In our implementation, the matrix elements of $\mathbb{V}^{\mathrm{iso}}$ replace the matrix elements H_{kl} for propagation of the TDSE in eqn (2), while the diabatic NACEs (presumably small) are ignored. For the calculation of physical forces on each nucleus, eqn (5), and NACVs, eqn (10), $\nabla_I \mathbb{H}$ is replaced by $\nabla_{I_\alpha} \mathbb{V}^{\mathrm{iso}}$. In addition, the adiabatic NACEs are obtained from the NACVs using eqn (7) and inserted in eqn (6) for calculation of the hopping probability. The rescaling of velocities following a successful jump is performed in the direction parallel to NACVs corresponding to the eigenvalue spectrum of $\mathbb{V}^{\mathrm{iso}}$.

2.5 Analytical rate constants

The semi-classical Marcus nonadiabatic Golden rule rate constant (k_{M}) expression for charge transfer is given by:[59]

$$k_{\mathrm{M}} = \left(\frac{2\pi}{\hbar}\right)\left\langle {H_{kl}}^2 \right\rangle \left(\frac{4\pi\lambda}{\beta}\right)^{-1/2} \exp\left(-\beta\frac{(\Delta A+\lambda)^2}{4\lambda}\right), \tag{30}$$

where H_{kl} is the electronic coupling between the diabatic states k and l, λ is the reorganization energy, and ΔA is the free energy difference between the two diabatic states. The quantum mechanical analog of the above equation has been derived by considering two electronic states in a bath of quantum harmonic oscillators (spin-boson):[60,61]

$$\begin{aligned} k_{\mathrm{LD}} = \left(\frac{\beta}{\hbar}\right)\left\langle {H_{kl}}^2 \right\rangle \int_{-\infty}^{+\infty} \mathrm{d}R \exp\Bigg(&-\left(\frac{\beta}{2}+\mathrm{i}\beta R\right)\Delta A \\ &-\frac{2}{\pi\hbar}\int_0^\infty \mathrm{d}\omega \frac{J(\omega)(\cosh(\beta\hbar\omega/2)-\cosh(\mathrm{i}R\beta\hbar\omega))}{\omega^2\sinh(\beta\hbar\omega/2)}\Bigg), \end{aligned} \tag{31}$$

where $J(\omega)$ is the spectral density function. The above equation can be further simplified for $\Delta A = 0$ using the saddle point approximation:[60–63]

$$k_{\mathrm{q}} \approx \left(\frac{2\pi}{\hbar}\right)\left\langle {H_{ij}}^2 \right\rangle \left(\frac{4\pi l_1}{\beta}\right)^{-1/2} \exp\left(-\beta\frac{l_2}{4}\right) \tag{32}$$

where

$$l_1 = \frac{\beta\hbar}{\pi}\int_0^\infty \mathrm{d}\omega\, J(\omega)\sinh^{-1}(\beta\hbar\omega/2) \tag{33}$$

and

$$l_2 = \frac{8}{\beta\hbar\pi}\int_0^\infty \mathrm{d}\omega\, \frac{J(\omega)}{\omega^2}\tanh(\beta\hbar\omega/4). \tag{34}$$

In the classical limit, when $\beta\hbar\omega \ll 1$, both l_1 and l_2 reduce to classical reorganization energy, λ, which is directly related to the spectral density function.

$$\lambda = \frac{2}{\pi}\int_0^\infty \mathrm{d}\omega\, \frac{J(\omega)}{\omega} \tag{35}$$

2.6 Charge transfer rate constant from the decay of diabatic population and surface hopping rate constant

We calculate the time-dependent diabatic population from the square of the expansion coefficient of the initial diabatic state, averaged over several SH trajectories at a given instant of time.

$$P_a(t) = \langle |u_a|^2 \rangle (t) \tag{36}$$

The decay of the diabatic population may be fitted to an exponential of the following form:

$$P_a(t) = a(\exp(-k_d t) - 1) + 1. \tag{37}$$

The prefactor "a" can be determined beforehand from the free energy difference, ΔA, between the initial and final states and the temperature (as done here) or can be considered as a fitting parameter.

For a reversible reaction where the reactant, X, transforms into a product, Y, with k_f and k_b as the forward and backward rate constants respectively, the decay of the population of X is given by

$$P_X(t) = \frac{k_f}{k_f + k_b}\left[\exp\left(-(k_f + k_b)t\right) - 1\right] + 1. \tag{38}$$

Comparing eqn (37) and (38), we get:

$$k_d = k_f + k_b \tag{39}$$

$$a = \frac{k_f}{k_f + k_b} = \frac{k_f}{k_d}. \tag{40}$$

Using the detailed balance relation ($k_f = k_b \exp(-\beta \Delta A)$), one obtains an expression for "a" in terms of ΔA while the surface hopping rate constant, k_{SH}, can be written in terms of k_d and "a".

$$a = \frac{1}{1 + \exp(\beta \Delta A)} \tag{41}$$

$$k_{SH} \equiv k_f = a k_d \tag{42}$$

3 Simulation details

3.1 Model system

We have investigated the rate constant for hole transfer in a dimer of ethylene-like molecules (ELMs), embedded in a bath of 124 neon atoms. The center of mass of the two ELMs is restrained with a weak restraining potential centered at 3.6 Å (force constant = 1.12 kcal mol^{-1} Å^{-2}). A similar model system with different simulation parameters was chosen in our previous studies. We refer to the molecules as "ethylene-like" because only their nuclear geometries correspond to

real ethylene molecules. The reorganization energy λ and the constant C determining the magnitude of diabatic electronic couplings, H_{kl}, are taken to be 200 meV and 0.005 Ha respectively. This scaling factor corresponds to $\langle H_{kl}^2 \rangle^{1/2}$ of $\sim$15 meV. This choice of parameters, though arbitrary, conforms to the reorganization energies and electronic couplings usually seen in the organic semiconductors.[56] The Ne atoms take the role of a heat bath facilitating energy exchange with the ELMs while running the FOB-SH simulation in the NVE ensemble. This way we avoid introduction of artificial bias forces due to the thermostat. We used a cubic box of length 60 Å which corresponds to a density of 6.3×10^{-4} atoms Å^{-3}.

3.2 Force field parameters

We assume that the hole transfer is mediated by the HOMO orbitals of the ethylene molecules, φ_1 and φ_2, which are transformed into the orthogonal basis $\{\phi_i\}$ for the expansion of the charge carrier wavefunction according to eqn (1). The diagonal elements of the corresponding 2×2 electronic Hamiltonian H_{kk}, $k = 1,2$, are estimated using two classical potential energy functions (force fields). In force field 1, ELM 1 is positively charged and ELM 2 is neutral, giving the site energies H_{11} and the corresponding forces $\nabla_I H_{11}$. In force field 2, ELM 2 is positively charged and ELM 1 is neutral, giving the site energies H_{22} and the corresponding forces $\nabla_I H_{22}$. Intra-molecular interactions for the neutral ELM are taken from the Generalized Amber Force Field (GAFF).[64] The same intramolecular parameters are taken for the charged ELM except for the carbon–carbon bond length which was chosen to obtain a reorganization energy λ for electron hole transfer of 200 meV (at infinite donor–acceptor distance).[50] This requirement gave a carbon–carbon bond length of 1.387 Å for the charged ELM, compared to 1.324 Å for the neutral molecule. The intermolecular interaction between the ELMs and between ELM and Ne atoms is modeled by Lennard-Jones terms, with parameters taken from the GAFF database for neutral and charged ELMs and from ref. 65 for Ne and applying the Lorentz–Berthelot mixing rules. Electrostatic interactions in the form of fixed point charges do not significantly alter the energetics of this system because only one ELM carries a net charge and the other ELM and Ne are charge neutral. Hence, for convenience, electrostatic interactions were switched off. The off-diagonal element of the Hamiltonian, H_{12}, is calculated using the analytic overlap method (AOM).[57] Briefly, the HOMO orbitals of the ELMs, φ_1 and φ_2, are expanded in a minimum Slater basis of p orbitals and updated along the trajectory as described in detail in ref. 50. H_{12} is obtained *via* the simple linear relationship $H_{12} = CS_{12}$, with $S_{12} = \langle \varphi_1 | \varphi_2 \rangle$ calculated analytically. The coupling derivatives $d'_{I,12} = \langle \varphi_1 | \nabla_I \varphi_2 \rangle$ are obtained using finite differences of the AOM overlap and are used for the calculation of $\nabla_I H_{12}$ and $\mathbf{d}^{\mathrm{ad}}_{I,12}$. The NACEs d^{ad}_{12} are calculated similarly using finite differences. A detailed description of these calculations is given in ref. 50. The rate constants, extracted from FOB-SH and SH-RP-iso simulations, are computed as a function of energy bias applied artificially to the second diagonal element of the diabatic Hamiltonians. The applied bias ranged from 0 (no bias) to -400 meV. Additionally, the SH-RP-iso method requires assigning phases (signs) to the off-diagonal elements of the isomorphic Hamiltonian. In the original paper, these signs were obtained from the phase of the off-diagonal elements at the centroid position. Here, we assign the signs corresponding to the signs of the analogous off-diagonal elements of the average

diabatic Hamiltonian. Furthermore, since the square of the off-diagonal elements of the isomorphic Hamiltonian is a difference of two terms, eqn (28), it becomes negative in some cases during the simulation. In those cases, we reassign these values to zero.

3.3 Preparation of initial structures

3.3.1 Detailed balance. To investigate detailed balance in FOB-SH simulations, we prepared initial structures drawn from a thermally equilibrated distribution of positions, velocities and adiabatic states. We built the initial configuration from two ELMs in their energy-minimized geometry, surrounded by neon atoms positioned in a regular grid. The system is equilibrated to the particular temperature (200 K or 300 K) for 1 ns in the NVT ensemble using a Nosé–Hoover thermostat. At 300 K, 150 ps of Born–Oppenheimer molecular dynamics for both the ground (E_0) and excited (E_1) adiabatic electronic state of the charged system is carried out using forces calculated according to eqn (5). We remove the first 50 ps where the system equilibrates and use the last 100 ps of the ground state trajectories to calculate the free energy between ground and excited state, $\Delta A_{01} = -(1/\beta)\ln\langle\exp[-\beta(E_1 - E_0)]\rangle_{E_0}$. The corresponding "exact" excited state population is determined as $P_1 = 1/(1 + \exp(\beta\Delta A_{01}))$, which will serve as reference values for the excited state population obtained from FOB-SH. We extracted $600(1 - P_1)$ configurations (nuclear coordinates and velocities) from the last 100 ps of the ground state run and $600P_1$ configurations from the last 100 ps of the excited state run as starting configurations for the FOB-SH runs, to ensure exact excited state population at the start of the run (at $t = 0$). The electronic wavefunction is initialized in the corresponding adiabatic state $\Psi(0) = \psi_0$ or ψ_1. A similar strategy was employed at 200 K but we needed a much longer (500 ps) simulation time to converge the excited state population. Out of 500 ps, structures were collected from the last 200 ps of simulation.

For investigation of detailed balance with SH-RP-iso, RPSH-BA, and RPSH-wBA methods a similar protocol is followed using the quantum free energy difference from RPMD simulation as a reference. To this end, 500 ps of path integral Langevin equation (PILE)[66] thermostating is followed by 150 ps or 500 ps of non-thermostatted Born–Oppenheimer RPMD simulation depending on whether the temperature is 300 K or 200 K. We remove the first 50 ps (300 ps for 200 K) where the system equilibrates and use the last 100 ps (200 ps for 200 K) of the ground state trajectories to calculate the quantum free energy between ground and excited state, $\Delta A_{01} = -(1/\beta)\ln\left[(1/n)\sum_{\alpha=1}^{n}\langle\exp[-\beta(E_{1,\alpha} - E_{0,\alpha})]\rangle_{E_{0,\alpha}}\right]$. We used 24 and 16 beads for the RPMD simulations at 200 K and 300 K respectively.

3.3.2 Rate constants and internal consistency. For investigation of internal consistency and calculation of rate constants from SH simulations, we initialize the trajectories in a slightly different fashion compared to the procedure described in the previous section. We start from the final geometry of the NVT (or PILE) equilibration on the first diabatic surface where ELM 1 is charged and ELM 2 is neutral and then perform 200 ps of NVE (or RPMD) simulation with no additional applied bias. The initial geometries for FOB-SH (or SH-RP-iso) trajectories were collected at regular intervals from the last 100 ps of NVE (or RPMD) equilibration. To investigate the effect of applied bias ($\Delta A < 0$) on rate constants

extracted from SH simulations, we employ the same initial structures but add the bias to the second diagonal element of the electronic Hamiltonian during the SH run. In this equilibration procedure, the NVE (or RPMD) simulation was run on a single diabatic surface where the charge is localized on one ELM whereas for the investigation of detailed balance we performed NVE (or RPMD) equilibration on the ground Born–Oppenheimer surface. For the path integral-based simulations, we employed 16 beads at 300 K, 24 beads at 200 K, 32 beads at 150 K and 48 beads at 100 K. The electronic wavefunction, in these simulations, is initialized in the first diabatic state whereas for nuclear dynamics the initial adiabatic state was chosen randomly based on the projection of the first diabatic state on a particular adiabatic state. While adiabatic and surface populations were calculated to investigate the internal consistency, the rate constants were extracted from the decay of the diabatic population as described later. We calculate the adiabatic population ($P_i^{\mathrm{ad}}(t)$) from the square of the adiabatic expansion coefficients (c_i) that are computed from the transformation matrix of eqn (4) and diabatic expansion coefficients of eqn (1). The surface population ($P_i^{\mathrm{surf}}(t)$) is defined as the fraction of the trajectories that are running on a particular adiabatic surface i.

$$P_i^{\mathrm{ad}}(t) = \langle |c_i|^2 \rangle (t) \tag{43}$$

$$P_i^{\mathrm{surf}}(t) = \frac{N_i(t)}{N_{\mathrm{tot}}} \tag{44}$$

The reorganization energy λ in eqn (30) is extracted from the distribution of the vertical energy gap in the reactant state sampled with classical MD simulations. The same value is also obtained when the reorganization energy is calculated from the spectral density function, eqn (35). The spectral density function $J(\omega)$ is obtained from the cosine transform of the diabatic energy gap autocorrelation function, which is calculated with classical MD simulations at a particular temperature.[63] $J(\omega)$ is also employed to compute the quantum rate constant, eqn (32).

3.4 SH simulations

FOB-SH simulations were carried out using a modified version of the CP2K simulation package. We generated 600 independent trajectories for each set of parameters investigated for FOB-SH starting from initial structures that were prepared employing the protocols described in Section 3.3. Unless stated otherwise, simulations have been carried out with the following default settings. The nuclear dynamics is propagated with the velocity-Verlet algorithm with forces calculated according to eqn (5) with a MD time step $\Delta t = 0.1$ fs. The simulations are run in the NVE ensemble with the temperature remaining approximately constant around the target temperature due to interaction with the bath of Ne atoms. Surface-hopping probabilities are calculated according to eqn (6) at every MD time step. The probability for a hop from the current state to the state closest in energy is replaced by the expression dictated by the self-consistent FSSH method[10] as described in our previous work.[58] We calculated the kinetic energy along the adiabatic NACV, eqn (10), to determine whether a hop was energy-allowed. Whenever a hop was energy-forbidden the velocities were always reversed according to the protocol described in our earlier work.[58] The

wavefunction of the excess charge carrier, eqn (1) was propagated by integrating eqn (2) using the Runge–Kutta algorithm of 4th order and an electronic time step $\delta t = \Delta t/5 = 0.02$ fs. An interpolation scheme is used to calculate the Hamiltonian matrix elements at each electronic time step, as explained in our previous work.[50] It is well documented that SH simulations suffer from an overcoherence problem.[67,68] Several decoherence correction schemes have been suggested over the years. In this work, we employ exponential damping of the inactive electronic adiabatic states following the energy-based decoherence correction scheme suggested by Truhlar *et al.*[7,69]

$$c_i \rightarrow c_i \exp(-\Delta t/\tau_{ia})$$
$$\tau_{ia} = \frac{\hbar}{|E_i - E_a|}\left(C + \frac{E_0}{T_a}\right) \tag{45}$$

For all our simulations we set $C = 1$ and $E_0 = 0.0$ Ha. We found that excited state populations are well converged within 30 ps at 300 K while a much longer time (∼50–100 ps) is required for simulations at lower temperatures. Error bars were determined by block averaging of the trajectories with a block size of ∼200 independent trajectories.

RPSH-BA, RPSH-wBA and SH-RP-iso simulations were carried with a similar protocol as above. We employ 1000 independent trajectories and calculated forces on the adiabatic surface determined by the potential energy matrix (electronic Hamiltonian) as defined in Sections 2.2, 2.3 and 2.4. All other settings including the MD time step, time step for propagation of the electronic Schrödinger equation and decoherence correction scheme are kept the same as above.

4 Results and discussion

4.1 Internal consistency and detailed balance

Two important desirable properties of any SH simulation are internal consistency and ability to maintain detailed balance in the long time limit. Internal consistency can be measured by the time-averaged root mean square error (RMSE) between the surface population $P_i^{\text{surf}}(t)$, eqn (44) and adiabatic population $P_i^{\text{ad}}(t)$, eqn (43).

$$\text{RMSE} = \left(\frac{1}{\tau}\int_0^{\tau}\left(P_1^{\text{surf}}(t) - P_1^{\text{ad}}(t)\right)^2\right)^{\frac{1}{2}} \tag{46}$$

RMSE for SH simulations with different methods employed in this study are shown in Fig. 1A. Overall, the internal consistency is found to be reasonable for all the simulations. The smallest and largest RMSE are found for the RPSH-BA and RPSH-wBA methods respectively, while RMSE for the FOB-SH and SH-RP-iso simulations fall in between the two. Moreover, the RMSE decreases with decrease in temperature for the FOB-SH method but increases with decrease in temperature for SH-RP-iso and RPSH-wBA simulations. Note that a certain percentage of the error is introduced due to approximate treatment of the overcoherence problem in SH simulations. The significantly lower RMSE for RPSH-BA

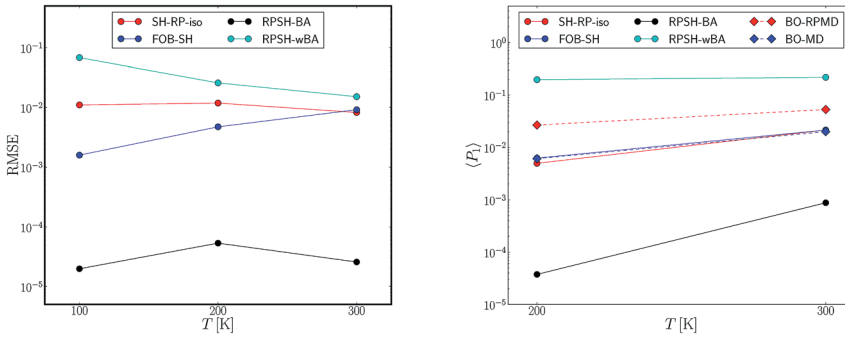

(A) RMSE in internal consistency vs. temperature

(B) Excited state population vs. temperature

Fig. 1 Root mean square error (RMSE) in internal consistency (eqn (46)), and excited state population calculated for a charge transfer reaction in an ELM dimer in a bath of Ne atoms. The excited state populations obtained with different methods are compared to the "exact" population computed with Born–Oppenheimer dynamics as described in Section 3.3.1.

is slightly misleading. A closer inspection of the results reveals that for RPSH-BA, the time-averaged surface population $\langle P_1^{\text{surf}} \rangle$ as well as the time-averaged adiabatic population $\langle P_1^{\text{ad}} \rangle$ are both significantly smaller than the equivalent quantities in FOB-SH simulations (0.001 *vs.* 0.017 and 4×10^{-6} *vs.* 0.025 respectively, at 300 K) resulting in smaller RMSE.

A comparison between the excited state population obtained from different SH-based simulations and from Born–Oppenheimer simulation on the ground adiabatic surface, as explained in Section 3.3.1, is shown in Fig. 1B. FOB-SH simulations exhibit excellent detailed balance with respect to the BO-MD reference values, while the excited state population obtained with the RPSH-BA method is found to be significantly smaller than the BO-RPMD reference values (0.027 and 0.053) at the two temperatures, 200 K and 300 K. With the RPSH-wBA method, the excited state population is overestimated at both 200 K (0.198) and 300 K (0.219). On the other hand, the SH-RP-iso method slightly underestimates the excited state population at both temperatures (0.005 and 0.02 respectively). The trend in the excited state population can be understood by inspecting the relative number of successful and rejected hops during SH simulations. In Fig. 2, we graphically plot the number of successful and rejected hops per trajectory for a simulation time of 5 ps at 300 K with the four different methods discussed in this work. It can be easily seen that the total number of attempted hops per trajectory is significantly higher for the RPSH-BA and RPSH-wBA methods compared to the SH-RP-iso and FOB-SH methods. The ratio of successful *vs.* rejected hops is, however, quite different for the two RPSH-based methods. For RPSH-BA simulations, only a very small percentage (0.26%) of the attempted hops are successful while for RPSH-wBA, 80.55% of the attempted hops are successful. In most cases, the attempted hops in RPSH-BA simulations are rejected due to lack of enough kinetic energy in the direction of the adiabatic NACV. Hence, the two RPSH-based methods either significantly underestimate or overestimate the excited state population. The percentage of successful hops is found to be quite similar for SH-RP-iso and FOB-SH, 54.29% and 48.34% respectively. Based on the

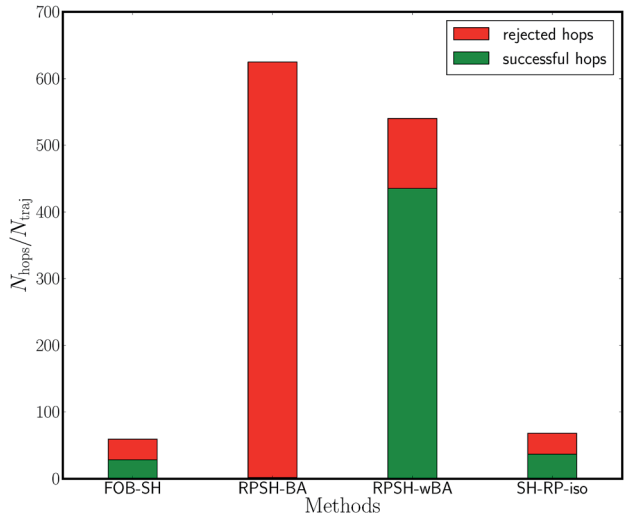

Fig. 2 Number of successful (green) and rejected (red) hops per trajectory at 300 K for different trajectory surface hopping-based methods employed in this study.

detailed balance performance we chose to compute the charge transfer rate constants with the FOB-SH and SH-RP-iso methods in Sections 4.2 and 4.3.

4.2 Temperature dependence of rate constant

In Fig. 3 we plot the rate constants obtained from SH simulations with the FOB-SH and SH-RP-iso methods at different temperatures. These rate constants are extracted from the decay of diabatic population as described in Section 2.6. In addition, we also plot the semi-classical (eqn (30)) and quantum (eqn (32)) charge transfer rate constants at different temperatures. The results obtained from FOB-SH simulations qualitatively follow the trend calculated with the semi-classical rate constant expression, Fig. 3, while the rate constants extracted from SH-RP-iso simulations are practically temperature-independent between 300 K and 100 K. This qualitatively different behavior of the classical and quantum nuclei can be understood in terms of the charge transfer barrier. In our system, the classical barrier for charge transfer, $\sim(\lambda/4 - \langle H_{kl}\rangle^{1/2})$, is small ($\sim$35 meV). This barrier is further reduced if one includes the ZPE correction, which is the case for the SH-RP-iso simulations. Hence, we speculate that the quantum nuclei can easily tunnel through this low barrier at low temperatures resulting in a rate constant which is approximately temperature-independent. The importance of nuclear tunneling at low temperatures can be assessed by comparing the mean radius of gyration, $\langle r_{T,i}\rangle$, of the atoms at 300 K and 100 K. The mean radius of gyration of all the atoms increases upon lowering the temperature (Fig. S1†). The nuclear quantum effects are further exaggerated if one compares the semi-classical *vs.* quantum rate constants. The semi-classical rate constant decreases with decreasing temperature as expected but the quantum rate constant increases with decreasing temperature. The temperature dependence of the two rate constants can be analyzed by considering the pre-exponential and exponential components

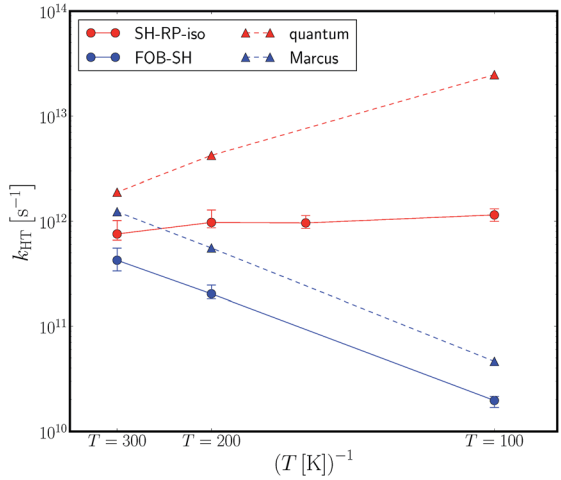

Fig. 3 Plot of rate constant *vs.* inverse temperature for charge transfer between two ELMs. The rate constants were extracted by fitting the decay of the diabatic population, obtained from FOB-SH and SH-RP-iso simulations, to an exponential function using eqn (37) and (42). These rate constants are compared with the results obtained from semi-classical (eqn (30)) and quantum (eqn (32)) rate constant expressions.

at zero driving force. For the same mean square electronic coupling ($\langle H_{kl}^2 \rangle$) parameter, the pre-exponential factor in the case of the quantum rate constant, eqn (33), increases much more steeply with decrease in temperature compared to the equivalent term in the semi-classical expression, $T^{-1/2}$. For the quantum rate constant, the growth in the pre-exponential factor outcompetes the decay of the exponential term, which becomes temperature-independent in the limit $\beta \to \infty$. The interplay between these two terms leads to an effective increase in the quantum rate constant with the decrease in temperature.

4.3 Dependence of rate constant on driving force

We calculated the change in rate constants with the change in driving force at 300 K and 100 K. The calculated rate constants are plotted in Fig. 4 and 5, respectively. Overall, the rate constants extracted from SH-RP-iso trajectories are very similar in magnitude to the rate constants obtained from FOB-SH simulations at 300 K. With very low or very high driving force, we observe slightly enhanced rate constants from SH-RP-iso simulations compared to the rate constants obtained from FOB-SH simulations at the same driving forces. This enhancement in rate constant can be attributed to the lowering of the effective charge transfer barrier due to the presence of ZPE corrections in the path integral-based simulations. The rate constants from FOB-SH simulations are also in fair agreement with Marcus rate constants. At 100 K, we observe a prominent asymmetry in the curvature of the rate constants calculated from SH-RP-iso trajectories as a function of increasing driving force, compared to the results obtained from FOB-SH simulations. To demonstrate this feature clearly we have plotted inverted parabolas on top of the data obtained with both the SH-RP-iso and FOB-SH methods in Fig. 5. The slower rate of decrease of rate constant with the increase in driving force in

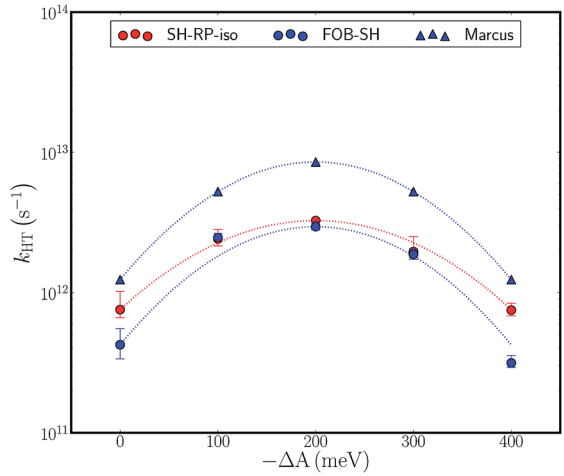

Fig. 4 Plot of rate constant *vs.* driving force at 300 K for hole transfer in an ELM dimer. Inverted parabolas are drawn on top of the rate constants obtained from FOB-SH and SH-RP-iso simulations as well as the rate constants computed with Marcus theory to emphasize the symmetry in the curvature of all the plots.

the Marcus "inverted" regime compared to the rate of increase in the normal regime has been demonstrated previously, and was attributed to vibrational tunneling.[70] The relative increase in radius of gyration upon increasing the driving force ($-\Delta A$) from 0 to 300 meV for the atoms of the two ELMs is ~1.5–3.0 times larger compared to the relative increase in the radius of gyration of the same atoms upon increasing the driving force from 0 to 400 meV at 300 K

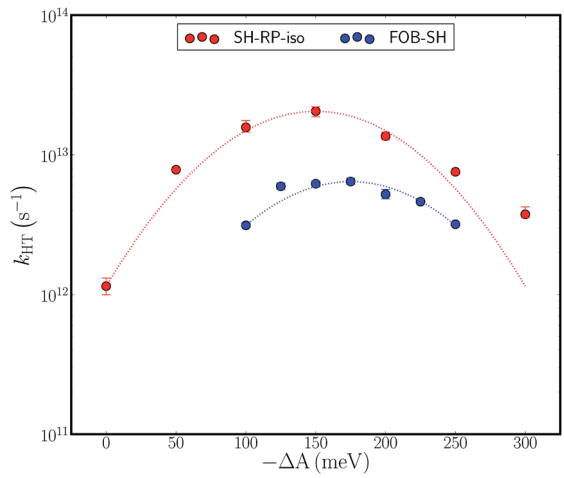

Fig. 5 Plot of rate constant *vs.* driving force at 100 K for hole transfer in an ELM dimer. Inverted parabolas, drawn on top of the rate constants, clearly demonstrate the asymmetry in the curvature of the plot of the rate constants obtained from SH-RP-iso simulations.

(Fig. S2†). In addition, we also observe a small shift in the maxima compared to the rate constants obtained from FOB-SH simulations. While a more extensive and systematic study comprising of systems either with several vibrational modes or with a higher charge transfer free energy barrier (equivalent to larger reorganizational energy) is required in order to fully comprehend the exact origin of this shift, we tentatively speculate that the shift is a consequence of varying extent of nuclear tunneling at different driving forces.

5 Conclusions

We have reported here the implementation of three different methods that include nuclear quantum effects in the context of nonadiabatic dynamics with a fragment orbital-based surface hopping propagation scheme in the CP2K software package. By comparing the excited state populations obtained from each of these simulations at different temperatures, we have shown that the results obtained with SH-RP-iso simulations deviate the least from the excited state populations obtained with the BO-RPMD method, while RPSH-BA and RPSH-wBA simulations either severely underestimate or overestimate the population in the excited adiabatic state. By analyzing the rate constants for charge transfer between two ethylene-like molecules in a bath of Ne atoms, we have shown that nuclear quantum effects are not of major importance at 300 K but become significant at lower temperatures. In future, we intend to compare the rate constants calculated with reactive flux formulation[71–73] with the rate constants computed here. Additionally, we aim at studying the temperature dependence of charge transport in more realistic systems, *e.g.* a chain of naphthalene molecules, employing the SH-RP-iso method.

Appendix

A Derivation of NACE expression in diabatic basis

Taking the derivative of the off-diagonal elements of the adiabatic electronic Hamiltonian, we get:

$$\begin{aligned}&\nabla_I\left[\mathbb{U}^\dagger\mathbb{H}\mathbb{U}\right]_{ij}\\&=\left[\left(\nabla_I\mathbb{U}^\dagger\right)\mathbb{H}\mathbb{U}\right]_{ij}+\left[\mathbb{U}^\dagger\nabla_I\mathbb{H}\mathbb{U}\right]_{ij}+\left[\mathbb{U}^\dagger\mathbb{H}(\nabla_I\mathbb{U})\right]_{ij}\\&=0.\end{aligned}$$

Hence,

$$\left[\mathbb{U}^\dagger\nabla_I\mathbb{H}\mathbb{U}\right]_{ij}=-\left[\left(\nabla_I\mathbb{U}^\dagger\right)\mathbb{H}\mathbb{U}\right]_{ij}-\left[\mathbb{U}^\dagger\mathbb{H}(\nabla_I\mathbb{U})\right]_{ij}. \tag{A.1}$$

Since the transformation matrix is unitary irrespective of nuclear configuration, we get:

$$\begin{aligned}&\nabla_I\left(\mathbb{U}^\dagger\mathbb{U}\right)=0\\&\nabla_I\mathbb{U}^\dagger=-\mathbb{U}^\dagger(\nabla_I\mathbb{U})\mathbb{U}^\dagger.\end{aligned} \tag{A.2}$$

The first term on the right hand side of eqn (A.1) is given by:

$$\begin{aligned}&\left[(\nabla_I \mathbb{U}^\dagger)\mathbb{H}\mathbb{U}\right]_{ij}\\&= \left[-\mathbb{U}^\dagger(\nabla_I \mathbb{U})\mathbb{U}^\dagger\mathbb{H}\mathbb{U}\right]_{ij}\\&= \left[-\left(\mathbb{U}^\dagger\nabla_I \mathbb{U}\right)\mathbb{H}^{\mathrm{ad}}\right]_{ij}\\&= -E_j\left[\mathbb{U}^\dagger\nabla_I \mathbb{U}\right]_{ij}.\end{aligned} \tag{A.3}$$

Similarly, the second term on the r.h.s. of eqn (A.1) is given by:

$$\begin{aligned}&\left[\mathbb{U}^\dagger\mathbb{H}(\nabla_I \mathbb{U})\right]_{ij}\\&= \left[\mathbb{U}^\dagger\mathbb{H}\left(\mathbb{U}\mathbb{U}^\dagger\right)(\nabla_I \mathbb{U})\right]_{ij}\\&= \left[\mathbb{H}^{\mathrm{ad}}\left(\mathbb{U}^\dagger\nabla_I \mathbb{U}\right)\right]_{ij}\\&= E_i\left[\mathbb{U}^\dagger\nabla_I \mathbb{U}\right]_{ij}.\end{aligned} \tag{A.4}$$

Substituting eqn (A.3) and (A.4) in eqn (A.1), we get:

$$\left[\mathbb{U}^\dagger\nabla_I\mathbb{H}\mathbb{U}\right]_{ij} = \left(E_j - E_i\right)\left[\mathbb{U}^\dagger\nabla_I \mathbb{U}\right]_{ij}. \tag{A.5}$$

Using the expression for adiabatic NACV in diabatic basis, eqn (9) and (A.5) we obtain the desired relation for adiabatic NACE, eqn (8).

$$\begin{aligned}d_{ij}^{\mathrm{ad}} &= \dot{\mathbf{R}}_I \cdot \mathbf{d}_{I,ij}^{\mathrm{ad}}\\&= \dot{\mathbf{R}}_\mathbf{I} \cdot \left(\frac{1}{E_j - E_i}\left[\mathbb{U}^\dagger\nabla_I\mathbb{H}\mathbb{U}\right]_{ij} + \left[\mathbb{U}^\dagger\mathbb{D}_I\mathbb{U}\right]_{ij}\right)\\&= \dot{\mathbf{R}}_\mathbf{I} \cdot \left(\left[\mathbb{U}^\dagger\nabla_I \mathbb{U}\right]_{ij} + \left[\mathbb{U}^\dagger\mathbb{D}_I\mathbb{U}\right]_{ij}\right)\\&= \left[\mathbb{U}^\dagger\dot{\mathbb{U}}\right]_{ij} + \left[\mathbb{U}^\dagger\mathbb{D}\mathbb{U}\right]_{ij}\end{aligned}$$

B RPSH-BA: electronic Schrödinger equation in diabatic basis

The vector-matrix form of eqn (13) is given by:

$$i\dot{\mathbf{c}} = \left(\tilde{\mathbb{H}}^{\mathrm{ad}} - \mathrm{i}\tilde{\mathbb{D}}^{\mathrm{ad}}\right)\mathbf{c} \tag{B.1}$$

where

$$\begin{aligned}\left[\tilde{\mathbb{H}}^{\mathrm{ad}}\right]_{ii} &= \left[\overline{\mathbb{U}}^\dagger\tilde{\mathbb{H}}\overline{\mathbb{U}}\right]_{ii} = \frac{1}{n}\sum_{\alpha=1}^{n} E_{i,\alpha}\\\left[\tilde{\mathbb{D}}^{\mathrm{ad}}\right]_{ij} &= \frac{1}{n}\sum_{\alpha=1}^{n} d_{ij}^{\mathrm{ad}}(\{\mathbf{R}_I\}_\alpha).\end{aligned} \tag{B.2}$$

Inserting eqn (15) in (B.1), we obtain:

$$i\left(\dot{\overline{\mathbb{U}}}^\dagger\mathbf{u} + \overline{\mathbb{U}}^\dagger\dot{\mathbf{u}}\right) = \left(\tilde{\mathbb{H}}^{\mathrm{ad}} - i\tilde{\mathbb{D}}^{\mathrm{ad}}\right)\overline{\mathbb{U}}^\dagger\mathbf{u}. \tag{B.3}$$

Rearranging eqn (B.3), inserting eqn (3) and (7) and multiplying from the left with $\overline{\mathbb{U}}$ we obtain eqn (16).

$$i\dot{\mathbf{u}} = \overline{\mathbb{U}}\left(\frac{1}{n}\sum_{\alpha=1}^{n}\mathbb{U}_{\alpha}^{\dagger}\mathbb{H}_{\alpha}\mathbb{U}_{\alpha}\right)\overline{\mathbb{U}}^{\dagger}\mathbf{u} - i\overline{\mathbb{U}}\left(\frac{1}{n}\sum_{\alpha=1}^{n}\left[\mathbb{U}_{\alpha}^{\dagger}\dot{\mathbb{U}}_{\alpha} + \mathbb{U}_{\alpha}^{\dagger}\mathbb{D}_{\alpha}\mathbb{U}_{\alpha}\right]\right)\overline{\mathbb{U}}^{\dagger}\mathbf{u} - i\overline{\mathbb{U}}\dot{\overline{\mathbb{U}}}^{\dagger}\mathbf{u} \quad \text{(B.4)}$$

C Derivation of NACV expression in RPSH-wBA

Let $|i\rangle$ and $|j\rangle$ be the eigenstates of the average electronic Hamiltonian, $\overline{H}$ with eigenvalues E_i and E_j:

$$\begin{aligned}&\nabla_{I_\alpha}\langle i|\overline{H}|j\rangle\\ &= \langle\nabla_{I_\alpha} i|\overline{H}|j\rangle + \langle i|\nabla_{I_\alpha}\overline{H}|j\rangle + \langle i|\overline{H}|\nabla_{I_\alpha} j\rangle\\ &= 0.\end{aligned} \quad \text{(C.1)}$$

Using the definition of adiabatic NACV,

$$\mathbf{d}^{\mathrm{ad}}_{I_\alpha,ij} = \langle i|\nabla_{I_\alpha} j\rangle = -\langle\nabla_{I_\alpha} i|j\rangle \text{ we obtain, } -E_j\mathbf{d}^{\mathrm{ad}}_{I_\alpha,ij} + \langle i|\nabla_{I_\alpha}(\overline{H})|j\rangle + E_i\mathbf{d}^{\mathrm{ad}}_{I_\alpha,ij} = 0. \quad \text{(C.2)}$$

Rearranging the terms, we get:

$$\begin{aligned}\mathbf{d}^{\mathrm{ad}}_{I_\alpha,ij} &= \frac{1}{\Delta E_{ij}}\langle i|\nabla_{I_\alpha}\overline{H}|j\rangle\\ &= \frac{1}{\Delta E_{ij}}\left(\frac{1}{n}\right)\left\langle i\left|\sum_{\alpha'}\nabla_{I_\alpha}H_{\alpha'}\right|j\right\rangle\\ &= \frac{1}{n\Delta E_{ij}}\sum_{\alpha'}\sum_{i_{\alpha'}}\sum_{j_{\alpha'}}\left\langle i|i_{\alpha'}\right\rangle\left\langle j_{\alpha'}|j\right\rangle\left\langle i_{\alpha'}\left|\nabla_{I_\alpha}H_{\alpha'}\right|j_{\alpha'}\right\rangle\end{aligned} \quad \text{(C.3)}$$

where the last line is obtained by inserting the completeness of the eigenstates of the electronic Hamiltonian of each individual bead.

Following Spencer *et al.*,[50] we can write an expression for the gradient of the electronic Hamiltonian in the diabatic basis of each individual bead:

$$\begin{aligned}&\left\langle i_{\alpha'}\left|\nabla_{I_\alpha}H_{\alpha'}\right|j_{\alpha'}\right\rangle\\ &= \left[\mathbb{U}_{\alpha'}^{\dagger}\mathbb{G}_{I_{\alpha\alpha'}}\mathbb{U}_{\alpha'}\right]_{i_{\alpha'}j_{\alpha'}}\\ &= \left[\mathbb{U}_{\alpha'}^{\dagger}\nabla_{I_\alpha}\mathbb{H}_{\alpha'}\mathbb{U}_{\alpha'}\right]_{i_{\alpha'}j_{\alpha'}} + \left[\mathbb{U}_{\alpha'}^{\dagger}\left[\mathbb{D}_{I_{\alpha\alpha'}},\mathbb{H}_{\alpha'}\right]\mathbb{U}_{\alpha'}\right]_{i_{\alpha'}j_{\alpha'}}\end{aligned} \quad \text{(C.4)}$$

where $[\mathbb{D}_{I_{\alpha\alpha'}}]_{k'l'} = \langle k'|\nabla_{I_\alpha} l'\rangle(\{k',l'\}\in\alpha')$. Inserting eqn (C.4) into eqn (C.3) we obtain an expression for adiabatic NACV in terms of gradient of Hamiltonian of each bead in diabatic basis. Following Carof *et al.*,[58] we can ignore the second term on the r.h.s. of eqn (C.4):

$$\mathbf{d}^{\mathrm{ad}}_{I_\alpha,ij} \approx \frac{1}{n\Delta E_{ij}}\sum_{\alpha'}\sum_{i_{\alpha'}}\sum_{j_{\alpha'}}\left\langle i|i_{\alpha'}\right\rangle\left\langle j_{\alpha'}|j\right\rangle\left[\mathbb{U}_{\alpha'}^{\dagger}\nabla_{I_\alpha}\mathbb{H}_{\alpha'}\mathbb{U}_{\alpha'}\right]_{i_{\alpha'}j_{\alpha'}}. \quad \text{(C.5)}$$

The above expression can be further simplified by assuming that the change in nuclear position in one bead does not affect the electronic Hamiltonian of

another bead. Hence, the triple sum in eqn (C.5) is reduced to a double sum over the eigenstates of the ath bead only, leading to eqn (26).

D Derivation of NACE expression in RPSH-wBA

$$\begin{aligned} d_{ij}^{\mathrm{ad}} &= \dot{\mathbf{R}}_{I,\alpha} \cdot \mathbf{d}_{I_\alpha,ij}^{\mathrm{ad}} \\ &= \dot{\mathbf{R}}_{I,\alpha} \cdot \left(\left[\mathbb{U}_{\alpha'}^{\dagger} \nabla_{I_\alpha} \mathbb{H}_{\alpha'} \mathbb{U}_{\alpha'} \right]_{i_{\alpha'} j_{\alpha'}} + \left[\mathbb{U}_{\alpha'}^{\dagger} \left[\mathbb{D}_{I_{\alpha\alpha'}}, \mathbb{H}_{\alpha'} \right] \mathbb{U}_{\alpha'} \right]_{i_{\alpha'} j_{\alpha'}} \right) \\ &= \Delta E_{i_{\alpha'} j_{\alpha'}} \dot{\mathbf{R}}_{I,\alpha} \cdot \left(\left[\mathbb{U}_{\alpha'}^{\dagger} \nabla_{I_\alpha} \mathbb{U}_{\alpha'} \right]_{i_{\alpha'} j_{\alpha'}} + \left[\mathbb{U}_{\alpha'}^{\dagger} \mathbb{D}_{I_{\alpha\alpha'}} \mathbb{U}_{\alpha'} \right]_{i_{\alpha'} j_{\alpha'}} \right) \\ &= \Delta E_{i_{\alpha'} j_{\alpha'}} \left(\left[\mathbb{U}_{\alpha'}^{\dagger} \dot{\mathbb{U}}_{\alpha'} \right]_{i_{\alpha'} j_{\alpha'}} + \left[\mathbb{U}_{\alpha'}^{\dagger} \mathbb{D}_{\alpha'} \mathbb{U}_{\alpha'} \right]_{i_{\alpha'} j_{\alpha'}} \right) \end{aligned} \tag{D.1}$$

Conflicts of interest

There are no conflicts to declare.

Acknowledgements

S. Ghosh and S. Giannini were supported by the European Research Council (ERC) under the European Union's Horizon 2020 research and innovation programme (grant agreement no. 682539/SOFTCHARGE). *Via* our membership of the UK's HEC Materials Chemistry Consortium, which is funded by EPSRC (EP/L000202), this work used the ARCHER UK National Supercomputing Service (http://www.archer.ac.uk). In addition, S. Ghosh wants to thank previous group member Antoine Carof for several discussions on surface hopping, Zdenek Futera for coding suggestions and Orestis Ziogos for fruitful discussions on different facets of science.

References

1 J. C. Tully and R. K. Preston, *J. Chem. Phys.*, 1971, **55**, 562–572.
2 J. C. Tully, *J. Chem. Phys.*, 1990, **93**, 1061–1071.
3 S. Hammes-Schiffer, J. C. Tully, S. Hammes-Schiffer, J. C. Tully, S. Hammes-Schiffer and J. C. Tully, *J. Chem. Phys.*, 1994, **101**, 4657–4667.
4 J. R. Schmidt, P. V. Parandekar and J. C. Tully, *J. Chem. Phys.*, 2008, **129**, 44104.
5 A. Jain, M. F. Herman, W. Ouyang and J. E. Subotnik, *J. Chem. Phys.*, 2015, **143**, 134106.
6 J. E. Subotnik and N. Shenvi, *J. Chem. Phys.*, 2011, **134**, 244114.
7 G. Granucci and M. Persico, *J. Chem. Phys.*, 2007, **126**, 134114.
8 A. Jain, E. Alguire and J. E. Subotnik, *J. Chem. Theory Comput.*, 2016, **12**, 5256–5268.
9 H. M. Jaeger, S. Fischer and O. V. Prezhdo, *J. Chem. Phys.*, 2012, **137**, 22A545.
10 L. Wang and O. V. Prezhdo, *J. Phys. Chem. Lett.*, 2014, **5**, 713–719.
11 L. Spörkel and W. Thiel, *J. Chem. Phys.*, 2016, **144**, 194108.

12 G. Granucci, M. Persico and A. Toniolo, *J. Chem. Phys.*, 2001, **114**, 10608–10615.
13 S. Fernandez-Alberti, A. E. Roitberg, T. Nelson and S. Tretiak, *J. Chem. Phys.*, 2012, **137**, 14512.
14 G. A. Meek and B. G. Levine, *J. Phys. Chem. Lett.*, 2014, **5**, 2351–2356.
15 L. Yue, L. Yu, C. Xu, Y. Lei, Y. Liu and C. Zhu, *ChemPhysChem*, 2017, **18**, 1274–1287.
16 A. K. Belyaev, C. Lasser and G. Trigila, *J. Chem. Phys.*, 2014, **140**, 224108.
17 W. Xie and W. Domcke, *J. Chem. Phys.*, 2017, **147**, 184114.
18 A. V. Akimov, D. Trivedi, L. Wang and O. V. Prezhdo, *J. Phys. Soc. Jpn.*, 2015, **84**, 94002.
19 L. Wang, D. Trivedi and O. V. Prezhdo, *J. Chem. Theory Comput.*, 2014, **10**, 3598–3605.
20 J. C. Tully, *Faraday Discuss.*, 1998, **110**, 407–419.
21 P. V. Parandekar and J. C. Tully, *J. Chem. Phys.*, 2005, **122**, 94102.
22 A. Bastida, C. Cruz, J. Zúñiga, A. Requena and B. Miguel, *Chem. Phys. Lett.*, 2006, **417**, 53–57.
23 D. V. Makhov, C. Symonds, S. Fernandez-Alberti and D. V. Shalashilin, *Chem. Phys.*, 2017, **493**, 200–218.
24 C. C. Martens and J.-Y. Fang, *J. Chem. Phys.*, 1997, **106**, 4918–4930.
25 R. Kapral and G. Ciccotti, *J. Chem. Phys.*, 1999, **110**, 8919–8929.
26 D. Mac Kernan, G. Ciccotti and R. Kapral, *J. Phys. Chem. B*, 2008, **112**, 424–432.
27 G. Stock and M. Thoss, *Phys. Rev. Lett.*, 1997, **78**, 578–581.
28 M. Thoss and G. Stock, *Phys. Rev. A*, 1999, **59**, 64–79.
29 N. Ananth, *J. Chem. Phys.*, 2013, **139**, 124102.
30 J. O. Richardson and M. Thoss, *J. Chem. Phys.*, 2013, **139**, 31102.
31 S. N. Chowdhury and P. Huo, *J. Chem. Phys.*, 2017, **147**, 214109.
32 M. Ben-Nun, J. Quenneville and T. J. Martínez, *J. Phys. Chem. A*, 2000, **104**, 5161–5175.
33 B. F. E. Curchod and T. J. Martínez, *Chem. Rev.*, 2018, **118**, 3305–3336.
34 I. Tavernelli, *Phys. Rev. A*, 2013, **87**, 42501.
35 B. F. E. Curchod, I. Tavernelli and U. Rothlisberger, *Phys. Chem. Chem. Phys.*, 2011, **13**, 3231.
36 F. Agostini, S. K. Min, A. Abedi and E. K. U. Gross, *J. Chem. Theory Comput.*, 2016, **12**, 2127–2143.
37 Y. Jiang, X. Zhong, W. Shi, Q. Peng, H. Geng, Y. Zhao and Z. Shuai, *Nanoscale Horiz.*, 2016, **1**, 53–59.
38 J. Zheng, R. Meana-Pañeda and D. G. Truhlar, *J. Phys. Chem. Lett.*, 2014, **5**, 2039–2043.
39 I. R. Craig and D. E. Manolopoulos, *J. Chem. Phys.*, 2004, **121**, 3368–3373.
40 I. R. Craig and D. E. Manolopoulos, *J. Chem. Phys.*, 2005, **122**, 84106.
41 S. Habershon, D. E. Manolopoulos, T. E. Markland and T. F. Miller, *Annu. Rev. Phys. Chem.*, 2013, **64**, 387–413.
42 A. R. Menzeleev, F. Bell and T. F. Miller, *J. Chem. Phys.*, 2014, **140**, 64103.
43 P. Shushkov, R. Li and J. C. Tully, *J. Chem. Phys.*, 2012, **137**, 22A549.
44 F. A. Shakib and P. Huo, *J. Phys. Chem. Lett.*, 2017, **8**, 3073–3080.
45 J. Lu and Z. Zhou, *J. Chem. Phys.*, 2017, **146**, 154110.
46 J. Lu and Z. Zhou, *J. Chem. Phys.*, 2018, **148**, 64110.
47 X. Tao, P. Shushkov and T. F. Miller, *J. Chem. Phys.*, 2018, **148**, 10237.
48 J. Cao and G. A. Voth, *J. Chem. Phys.*, 1993, **99**, 10070–10073.

49 J.-L. Liao and G. A. Voth, *J. Phys. Chem. B*, 2002, **106**, 8449–8455.
50 J. Spencer, F. Gajdos and J. Blumberger, *J. Chem. Phys.*, 2016, **145**, 064102.
51 H. Oberhofer, K. Reuter and J. Blumberger, *Chem. Rev.*, 2017, **117**, 10319–10357.
52 J. Spencer, L. Scalfi, A. Carof and J. Blumberger, *Faraday Discuss.*, 2016, **195**, 215–236.
53 S. Giannini, A. Carof and J. Blumberger, *J. Phys. Chem. Lett.*, 2018, **9**, 3116–3123.
54 N. Karl and J. Marktanner, *Mol. Cryst. Liq. Cryst. Sci. Technol., Sect. A*, 2001, **355**, 149–173.
55 T. Sakanoue and H. Sirringhaus, *Nat. Mater.*, 2010, **9**, 736–740.
56 H. Yang, F. Gajdos and J. Blumberger, *J. Phys. Chem. C*, 2017, **121**, 7689–7696.
57 F. Gajdos, S. Valner, F. Hoffmann, J. Spencer, M. Breuer, A. Kubas, M. Dupuis and J. Blumberger, *J. Chem. Theory Comput.*, 2014, **10**, 4653–4660.
58 A. Carof, S. Giannini and J. Blumberger, *J. Chem. Phys.*, 2017, **147**, 214113.
59 R. A. Marcus, *Rev. Mod. Phys.*, 1993, **65**, 599.
60 J. S. Bader, R. A. Kuharski and D. Chandler, *J. Chem. Phys.*, 1990, **93**, 230.
61 X. Song and R. A. Marcus, *J. Chem. Phys.*, 1993, **99**, 7768–7773.
62 P. Siders and R. A. Marcus, *J. Am. Chem. Soc.*, 1981, **103**, 741–747.
63 J. Blumberger and G. Lamoureux, *Mol. Phys.*, 2008, **106**, 1597–1611.
64 J. Wang, R. M. Wolf, J. W. Caldwell, P. A. Kollman and D. A. Case, *J. Comput. Chem.*, 2004, **25**, 1157–1174.
65 C. P. Herrero, *Phys. Rev. B*, 2001, **65**, 014112.
66 M. Ceriotti, M. Parrinello, T. E. Markland and D. E. Manolopoulos, *J. Chem. Phys.*, 2010, **133**, 124104.
67 O. V. Prezhdo and P. J. Rossky, *J. Chem. Phys.*, 1997, **107**, 5863–5878.
68 J. E. Subotnik, A. Jain, B. Landry, A. Petit, W. Ouyang and N. Bellonzi, *Annu. Rev. Phys. Chem.*, 2016, **67**, 387–417.
69 C. Zhu, A. W. Jasper and D. G. Truhlar, *J. Chem. Phys.*, 2004, **120**, 5543–5557.
70 P. Siders and R. A. Marcus, *J. Am. Chem. Soc.*, 1981, **103**, 748–752.
71 S. Hammes-Schiffer, J. C. Tully, S. Hammes-Schiffer and J. C. Tully, *J. Chem. Phys.*, 1995, **103**, 8528–8537.
72 A. Jain and J. E. Subotnik, *J. Chem. Phys.*, 2015, **143**, 134107.
73 X. Tao, P. Shushkov and T. F. Miller, *J. Phys. Chem. A*, 2019, **123**, 3013–3020.